processes

MDPI

Article

Quantitative Characterization of Shale Pores and Microfractures Based on NMR T_2 Analysis: A Case Study of the Lower Silurian Longmaxi Formation in Southeast Sichuan Basin, China

Chuxiong Li [1,2,*], Baojian Shen [1,3], Longfei Lu [1,2], Anyang Pan [1,2], Zhiming Li [1,2], Qingmin Zhu [1,4] and Zhongliang Sun [1,2]

[1] State Key Laboratory of Shale Oil and Gas Enrichment Mechanisms and Effective Development, Beijing 100083, China
[2] Wuxi Petroleum Geology Institute, Research Institute of Petroleum Exploration and Development, SINOPEC, Wuxi 214126, China
[3] Petroleum Exploration and Production Research Institute, SINOPEC, Beijing 100083, China
[4] Department of Science and Technology, SINOPEC, Beijing 100083, China
* Correspondence: lichuxiong.syky@sinopec.com

Abstract: In order to quantitatively characterize shale pores and microfractures, twelve marine shale samples from the Longmaxi Formation in the southeastern Sichuan Basin were selected and their NMR T_2 spectra were analyzed under the conditions of full brine saturation, cyclic centrifugal treatment and cyclic heat treatment. Then, movable, capillary bound and unrecoverable fluid of shale samples were distinguished and the NMR porosity and full-scale PSD were calculated. Based on NMR spectral peak identification, the relative content of pores and microfractures was determined and their influence factors were analyzed. The results show that the PSD of shale samples is bimodal, with pores distributed in the range of 1 nm to 200 nm and microfractures distributed in the range of 200 nm to 5000 nm, with relative contents in the ranges of 3.44–6.79% and 0.22–1.43%, respectively. Nanoscale organic pores are the dominant type of pores, while inorganic pores and microfractures contribute much less to the shale reservoir space than organic pores. The T_2 cutoff values range from 0.55 ms to 6.73 ms, and the surface relaxivities range from 0.0032 μm/ms to 0.0391 μm/ms. Their strong correlation with TOC suggests that organic matter is the main factor controlling the pore type and structure. In addition, the main difference between NMR porosity and He porosity is that gas logging porosity is used to detect connected pores, while NMR porosity also includes closed pores and microfractures. Combined with NMR and high-temperature pressure displacement experimental facilities, this will be a further step towards studying the pore structure of shale under simulated formation conditions.

Keywords: marine shale; nuclear magnetic resonance T_2 spectrum; pore size distribution; pore type; microfracture

Citation: Li, C.; Shen, B.; Lu, L.; Pan, A.; Li, Z.; Zhu, Q.; Sun, Z. Quantitative Characterization of Shale Pores and Microfractures Based on NMR T_2 Analysis: A Case Study of the Lower Silurian Longmaxi Formation in Southeast Sichuan Basin, China. *Processes* **2023**, *11*, 2823. https://doi.org/10.3390/pr11102823

Academic Editors: Keliu Wu, Mingjun Chen and Jiajia Bai

Received: 27 July 2023
Revised: 5 September 2023
Accepted: 5 September 2023
Published: 25 September 2023

1. Introduction

In recent years, the exploration and development technology of marine shale gas in China has developed rapidly, and the Jiaoshiba, Changning, Weiyuan and Zhaotong shale gas industrial development zones have been established successively, with the output of shale gas exceeding 26 billion m^3 in 2022 [1]. As an important index of shale gas reservoir evaluation, the microscopic pore structure of shale has been widely studied by many scholars [2–7]. At present, pore characterization techniques for shale reservoirs can be divided into three categories: image analysis techniques, fluid injection techniques and non-fluid injection techniques [8]. Image analysis technology is used to observe the characteristics of shale matrix and pore structure using micro-observation techniques such as optical microscopy, scanning electron microscopy (SEM) and atomic force microscopy (AFM) and

to obtain the image parameters through qualitative analysis [3–5,9,10]. The fluid injection technique is to inject inert gases such as N_2 and CO_2 or non-wetting fluids such as mercury into the pores of samples and to obtain pore structure parameters such as pore volume ratio and specific surface area through calculation of corresponding theoretical models, mainly including high-pressure mercury injection (MICP) and gas adsorption [11–13]. Non-fluid injection technology is based on a specific computational model or computer three-dimensional space modeling for the fine characterization of sample pore space, including micro–nano CT, small-angle X-ray scattering (SAXS) and nuclear magnetic resonance (NMR) [14–18]. However, a single technology often has the limitation of detection range and sample testing conditions, so the combination of multiple technologies is usually used to carry out the study of shale full-scale pore size distribution (PSD). In addition, although more and more experimental techniques have been applied to the characterization of pore structure, few techniques have been applied to the quantitative characterization of pore and microfracture integration.

NMR technology has the advantages of nondestructive analysis, large measurement range, high test accuracy, and simultaneously characterizing pores and microfractures of shale [16,19–21]. It has attracted the attention of an increasing number of researchers and has been gradually applied to shale oil and gas reservoir evaluation. Different from conventional reservoirs with relatively simple pore structure and easy expression of a fluid NMR signal, shale pore structure is relatively complex. Shale reservoir space can be divided into organic pores, inorganic pores and microfractures according to the genetic difference and contact relationship with the rock matrix [3–5,9]. Moreover, the pore size of shale varies unevenly from nano-sized pores to micro-sized fractures. Meanwhile, shale contains a lot of clay minerals and organic matter, resulting in matrix wettability differences [18,22,23]. The closed pore fluid in shale, hydrogen in organic matter, the development of paramagnetic minerals and other factors can cause interference in the process of NMR analysis [24,25]. These factors bring difficulties for the quantitative characterization of shale pore structure by NMR. Therefore, in the research process, the correct selection of NMR model parameters, the overcoming of water sensitivity of clay minerals and the accurate evaluation of pore and microfracture size distribution characteristics are key factors affecting the quality of NMR experiments in shale. However, a lack of comparative experiments causes problems in the validity of NMR results [16,23,26].

The main goal of this paper is to investigate the shale gas reservoir characteristics of the Lower Silurian Longmaxi Formation in southeast Sichuan basin using NMR experiments. We collected twelve shale samples and conducted a series of NMR experiments on full brine saturation, cyclic centrifugal treatment and cyclic heat treatment. According to the NMR T_2 spectral characteristics of shale in different water-bearing states, fluid types in shale pores were defined. Meanwhile, we calculated T_2 cutoff values and surface relaxivities, and analyzed types and distribution characteristics of shale pores and microfractures. Then, the differences between NMR porosity and He porosity were compared. The results could be helpful for the application of NMR techniques in the study of shale reservoirs and could provide a way to characterize quantitatively the complicated pore structure of shale oil and gas reservoirs.

2. Materials and Methods

2.1. Shale Samples

The experimental sample is from a deep shale gas exploration well in the Qijiang area, southeast of Sichuan Basin, China (Figure 1). Twelve shale core samples from the Longmaxi Formation of the Lower Silurian were selected vertically, using a drilling machine to drill plunger samples (about 2.54 cm in diameter) along the bedding plane for NMR experiments. The remaining cuttings were used in other experiments.

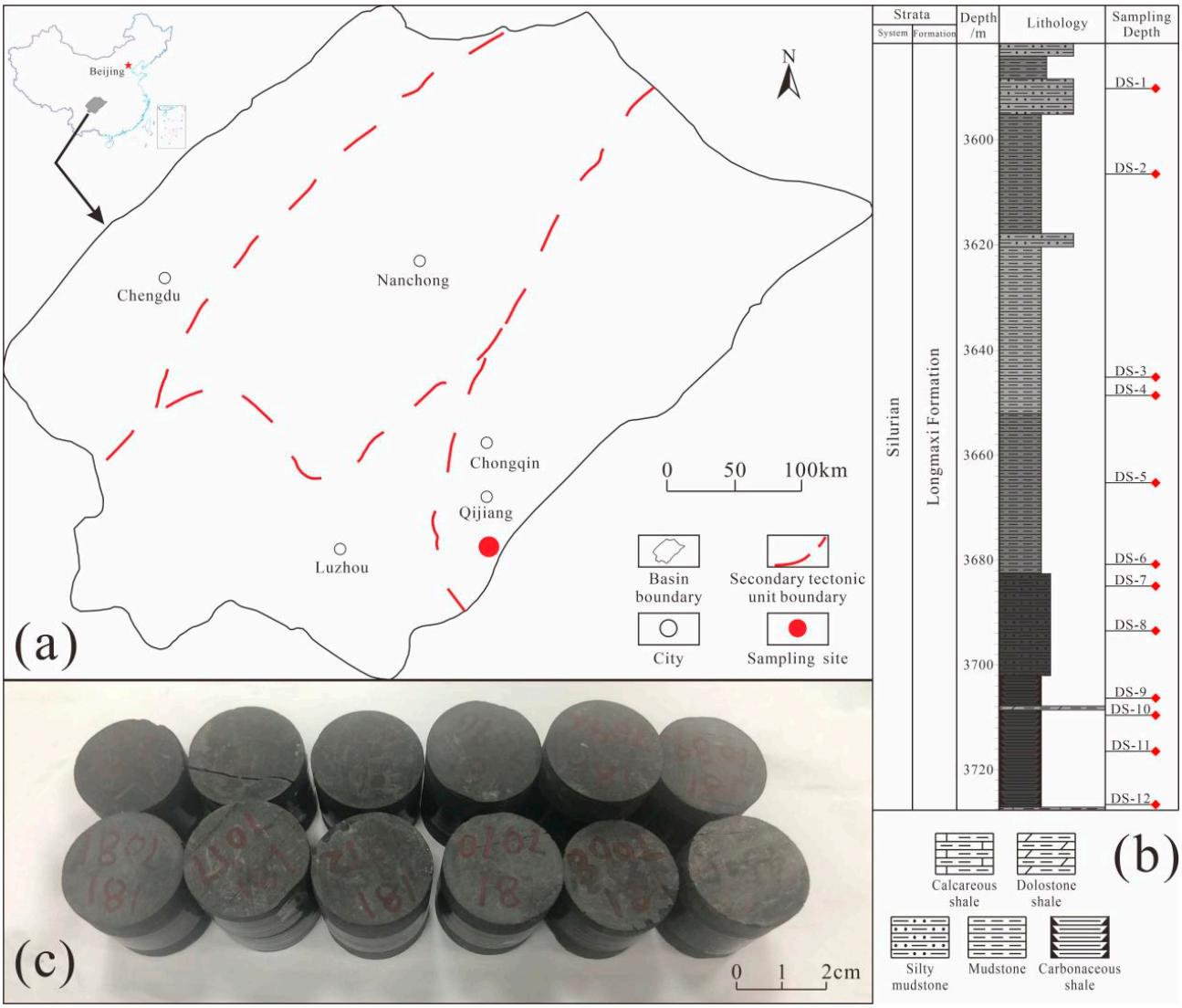

Figure 1. Shale samples and their sampling locations. (**a**) Sampling site; (**b**) stratigraphic column of Longmaxi Formation in southeast Sichuan Province; (**c**) photograph of twelve selected cylindrical shale samples for NMR measurements.

2.2. Principle and Measurements of NMR

NMR relaxation is based on mathematical inversion of the attenuation process of multistage echo string signals. The attenuation of a spin echo string is a function of detecting the number and distribution of hydrogen nuclei in a medium [27,28]. For a single type of porous rock medium, the transverse relaxation (T_2) mechanism of pore fluid can be regarded as a single exponential relaxation:

$$A(t) = A_o e^{-t/T_2} \quad (1)$$

where $A(t)$ is the nuclear magnetic signal of a test sample in time period t; T_2 is the NMR transverse relaxation time, ms.

The echo amplitude decreases with an increase in test time, so the attenuation information is used to determine the pore structure parameters [14,19]. A sample with a relatively high peak value in the NMR T_2 spectrum may have greater porosity, while the presence of multi-peak or wide-peak characteristics may represent diverse pore types or

structures [19,21,26]. The T_2 characteristics of fluids in porous media can be expressed by the following mathematical equation:

$$\frac{1}{T_2} = \frac{1}{T_{2B}} + \frac{1}{T_{2D}} + \frac{1}{T_{2S}} \quad (2)$$

where T_{2B}, T_{2D} and T_{2S} are bulk relaxation time, diffusion relaxation time and surface relaxation time, respectively. In low-field NMR experiments, the applied magnetic field is relatively uniform, and T_2 is generally contributed by T_{2S}, while the contribution of T_{2B} and T_{2D} can be ignored [16]. Therefore, without considering the T_{2B} and T_{2D} of pore fluid, Equation (2) can be simplified as:

$$\frac{1}{T_2} \approx \frac{1}{T_{2S}} = \rho_2 \frac{S}{V} \quad (3)$$

where ρ_2 is the surface relaxivity, μm/ms; S is the pore surface area, μm^2; and V is the pore volume, μm^3.

Since the surface relaxation mechanism acts on fluid medium in rock pores, its strength is usually related to the type of fluid medium, the wettability of the rock matrix, and the pore structure and distribution characteristics of the rock [16]. As can be seen from Equation (3), the essence of studying shale reservoir characteristics based on NMR technology is to analyze the different occurrence states of hydrogen-containing fluid in shale by using the surface relaxation characteristics of hydrogen-containing fluid in shale pores and fissures. Therefore, T_2 characteristics can be used to study the interaction mechanism between fluid and rock and to characterize the microscopic pore structure of shale.

In this study, the pretreatment process of the NMR experimental samples was full brine saturation, cyclic centrifugal treatment and cyclic heat treatment. First, the shale plunger samples were dried at 100 °C for 24 h and then placed in a saturated device for 1 h to remove water, air and adsorbent impurities. Subsequently, the samples were saturated with 3% KCl solution at 30 MPa fluid pressure for 48 h. Brine can effectively reduce the water sensitivity of clay minerals in shale [26], which is considered to be able to enter all connected pores under strong saturation pressure [29]. Next, the fully saturated samples were centrifuged in a constant temperature centrifuge, and the centrifugal speeds were set at 6000 rpm, 8000 rpm, 10,000 rpm and 12,000 rpm, respectively, with a single centrifugation time of 1 h. Finally, the centrifuged samples were dried at 60 °C, 80 °C, 100 °C and 120 °C, successively, with a single drying time of 24 h. According to the above pretreatment process, NMR analyses were conducted to obtain T_2 spectra of samples in different water states.

The NMR experimental instrument was MesoMR23/12-060H-I manufactured by the Suzhou Niumag company, Suzhou, China. The magnetic field intensity was 0.3 ± 0.03 T, and the resonance frequency was 12 MHz. The Carr–Purcell–Meiboom–Gill echo sequence was used for NMR T_2 analysis, and the measurement parameters were as follows: echo spacing, 0.2 ms; echo number, 10,000; waiting time, 6000 ms; and number of scans, 64.

2.3. Other Analyses

Cuttings samples were used for experiments of basic petrophysical and geochemical properties, including the TOC content, mineral content and helium porosity. Field emission scanning electron microscopy (FE-SEM) imaging of shale samples was performed using the Helios NanoLAB 650 (FEI Company, Hillsborough, OR, USA) field emission scanning electron microscope. Before FE-SEM observation, one surface of each sample was polished using the Leica EM TIC3X argon-ion polisher. Then, the polishing surface was coated with a gold film of 5 nm thickness to enhance the conductivity. Secondary electron modes and back-scattering electron modes were chosen to observe the different cross sections for each shale sample at various magnification scales.

3. Results

3.1. Characteristics of Shale Samples

The samples are gray-black shale with dense rock structure (Figure 1c). Lithologically, the shale samples are dominated by mudstone and carbonaceous shales. Mineralogically, quartz, clay minerals and carbonate minerals are the dominant minerals in the shale samples (Table 1). Quartz content is in the range of 23.9–69.1%, with an average of 39.8%. Clay mineral content is in the range of 15.1–54.0%, with an average of 31.44%. Carbonate minerals are mainly composed of calcite and dolomite, in the range of 5.8–24.7%, with an average of 12.4%.

Table 1. TOC and mineral composition information of shale samples.

Sample	Depth (m)	TOC	Quartz	Clay	Potash Feldspar	Plagioclase	Calcite	Dolomite	Ferrodolomite	Siderite	Pyrite
		(wt %)									
DS-1	3590.16	0.62	23.9	44.9	1.2	5.2	17.3	6.5			1.0
DS-2	3606.59	0.62	28.8	37.4	1.0	6.1	10.4	14.3		0.5	1.5
DS-3	3645.18	0.83	28.2	54.0		5.4	7.2	3.7		0.3	1.2
DS-4	3648.60	0.90	37.6	43.5		6.9	7.2	2.9		0.8	1.1
DS-5	3665.63	1.00	40.5	42.6		6.3	5.7	2.9			2.0
DS-6	3680.75	1.17	36.3	44.5		9.1	4.8	2.9		0.3	2.1
DS-7	3685.15	1.29	34.3	48.7		8.0	4.1	2.3		0.5	2.1
DS-8	3693.75	1.27	30.0	39.7	2.8	9.5	5.3	11.5		0.1	1.1
DS-9	3706.29	2.33	44.4	30.0	1.7	9.0	6.3	5.3		0.4	2.9
DS-10	3709.54	2.29	43.6	35.5	2.5	6.8	6.0	0.9	2.2	0.2	2.3
DS-11	3716.23	2.99	61.4	15.8		6.3	8.5	4.3		0.4	3.3
DS-12	3726.75	4.66	69.1	15.1		7.5	2.9	2.9		0.9	1.9

A previous study has shown that the Longmaxi shale in this area is in the over-mature stage, and the equivalent vitrinite reflectance is more than 2.5% [30]. The TOC content of the shale samples ranges from 0.62% to 4.66%, which gradually increases with an increase in burial depth (Table 1). Meanwhile, with an increase in burial depth, the content of quartz increases, the content of clay minerals decreases, and the content of carbonate minerals has no obvious change (Figure 2a). In addition, the TOC content has a good positive correlation with quartz content and a negative correlation with clay mineral content, but no obvious correlation with carbonate mineral content (Figure 2b). This is because the Lower Silurian Longmaxi shale in the Dingshan area is a shallow–deep-water shelf sedimentary environment, which is continuously distributed longitudinally, and quartz mainly comes from siliceous organisms [30,31]. Due to the high abundance of siliceous organisms at the bottom of the Longmaxi Formation, a large number of biological fossils such as graptolites and radiolaria can be seen in the shale, so the TOC content of the shale samples at corresponding locations is relatively high [31].

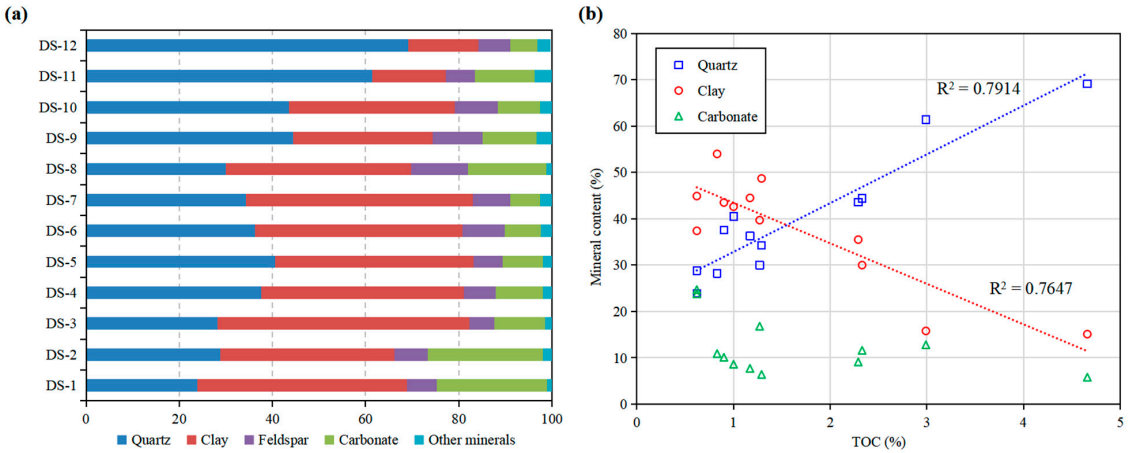

Figure 2. Mineral content of shale samples (**a**) and its correlation with TOC (**b**).

3.2. NMR Measurements

According to the principle of NMR experiment, the T_2 spectra of shale samples in a saturated fluid state can reflect the distribution characteristics of shale pores and microfractures [18,20]. The results of [20] demonstrated that the NMR T_2 spectral peak of organic pores is less than 3 ms, inorganic pores are 3–50 ms and microfractures are above 50 ms. Figure 3 shows the T_2 spectrum results of shale samples measured under full brine saturation, cyclic centrifugal treatment and cyclic heat treatment. It can be seen that the T_2 spectra of shale samples under saturation present a typical bimodal distribution, with a left peak at 0.01–20 ms and a right peak at 3–300 ms. Based on the distribution characteristics of the T_2 spectral peaks, it is considered that the left peak mainly represents pores and the right peak mainly represents microfractures. This indicates that there are more small pores in the shale, and the proportion of large pores and microfractures is relatively low. In addition, the low point between the two peaks is close to 0 in the ordinate, so the continuity of the two peaks is poor.

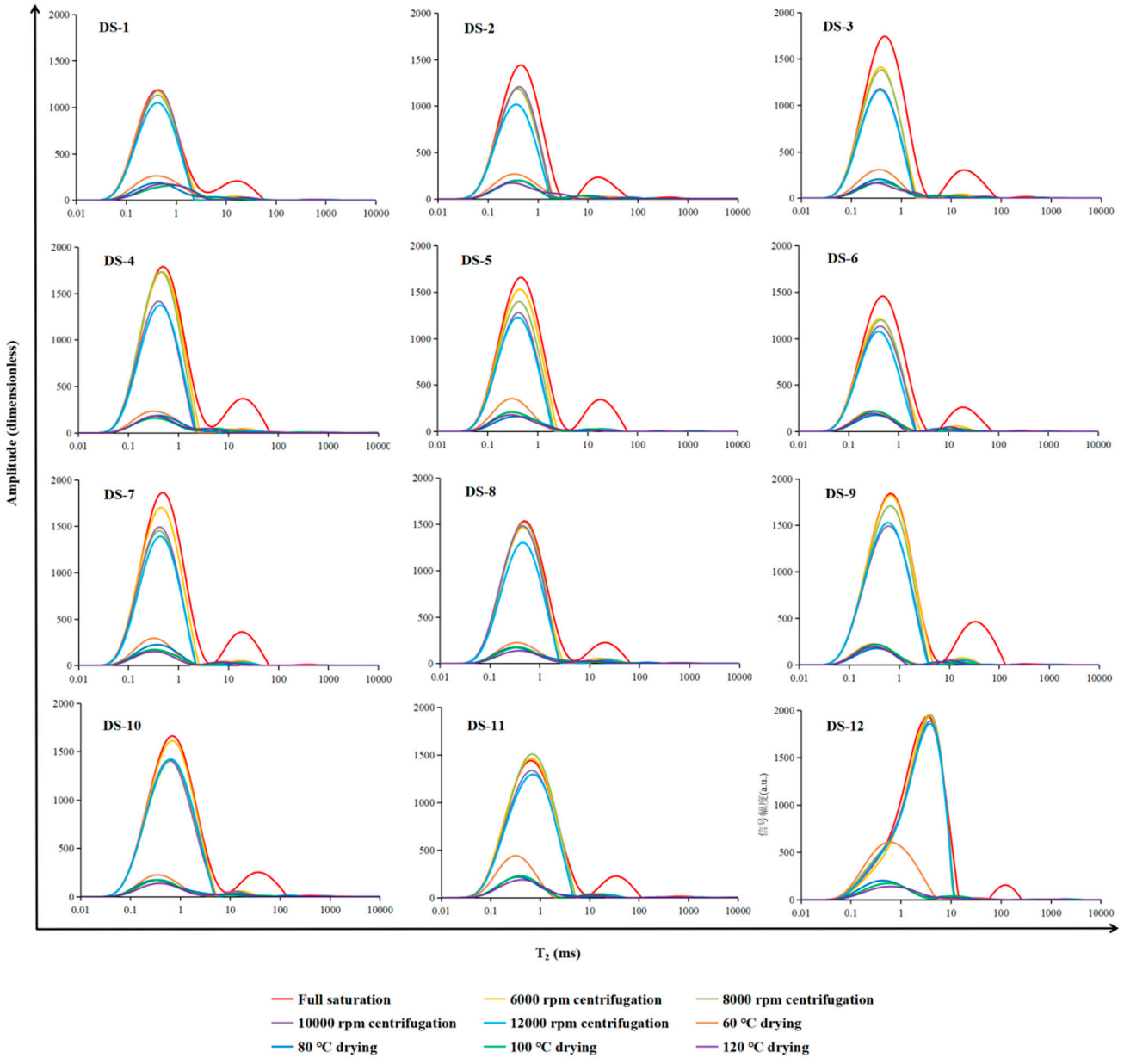

Figure 3. NMR T_2 spectra of shale samples in different conditions.

Fluid migration during centrifugation was analyzed by comparing the NMR T_2 spectra of shale samples after saturation and centrifugation. With an increase in centrifugal speed, the centrifugal pressure gradually increases and the signal amplitude and peak area of the T_2 spectra gradually decrease. Similarly, the right peak of the T_2 spectra disappears after centrifugation, indicating that the fluid in some of the larger pores and microfractures is almost completely removed during centrifugation. The difference is that the left peak of some samples is gradually shifted to the left while decreasing, showing that the fluid in the large pores is gradually expelled while that in the small pores is retained. However, even under the conditions of high rotational speed centrifugation, the fluid in pores cannot be completely expelled and the left peak of the T_2 spectra of the shale samples is still retained. This part of the NMR signal comes mainly from bound fluids subject to pore capillary forces and unable to be expelled by centrifugal experiments, unrecoverable fluids in closed pores and hydrogen in organic matter.

Furthermore, capillary bound and unrecoverable fluids are distinguished by looking at the variation in the T_2 spectra as the drying temperature is gradually increased. The signal amplitude of the dried sample is significantly reduced compared to centrifugation, and the position of the left peak has not shifted. However, the decreasing amplitude of the left peak changes little with increasing temperature. The signal amplitude at 60 °C is significantly higher than that at other temperature points, while the T_2 spectrum at 80–120 °C is relatively coincident. This suggests that when the temperature rises to a certain point, the capillary bound fluid in the shale sample is completely removed, and then the T_2 spectrum does not change due to the temperature rise, even if heating continues.

3.3. FE-SEM Observations

Pore and microfracture development characteristics of shale samples from different horizons were compared by FE-SEM (Figure 4). According to the classification scheme, shale pores are divided into organic pores, inorganic pores and microfractures, and inorganic pores are further divided into intergranular pores and intragranular pores [4]. Above all, micro-scale fractures are observed in the 300-fold view range, and they are distributed horizontally along the bedding plane (Figure 4a,e,i). Compared with DS-1, the organic matter in DS-12 is significantly more distributed, and amorphous organic matter and large organic matter particles densely distributed at the edges of mineral particles can be observed, while only sporadic organic matter can be observed in DS-1, while the content and distribution of organic matter in DS-8 are intermediate (Figure 4b,f,j). By further enlarging the field of view, a large number of spongy organic pores and a small number of intergranular pores can be observed (Figure 4c,d,g,h,k,l), and organic pores are the main pore type in the shale samples. This is consistent with the research results of [6], indicating that the pore types of Longmaxi Formation deep shale have little difference compared with middle–shallow shale. On the basis of the connectivity between pores, microfractures developed in bedding can be used as an effective channel for internal fluid migration and increase the connectivity between pores [32].

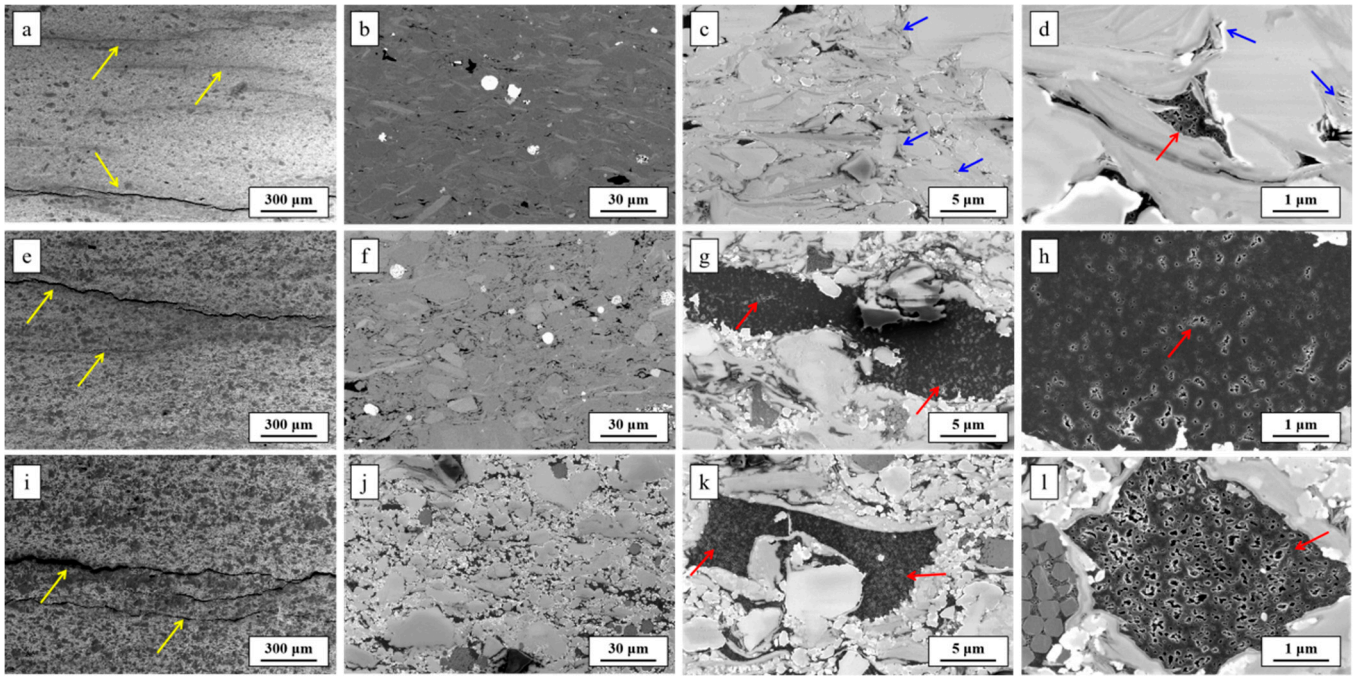

Figure 4. FE-SEM images of pores and microfractures in shale samples. The magnifications in (**a**–**d**), (**e**–**h**) and (**i**–**l**) are 300 times, 3000 times, 20,000 times and 80,000 times, respectively. Yellow arrows point to microfractures, blue arrows point to inorganic pores and red arrows point to organic pores.

4. Discussion

4.1. Fluid Type Classification and T_2 Cutoff Values

According to fluid mobility, fluid in shale can be divided into movable, capillary bound and unrecoverable fluid [24,26,33]. As shown in Figure 5, with an increase in centrifugal speed, the NMR signal frequency of shale samples gradually decreases, and the decreasing range becomes smaller, indicating that the movable fluid is almost completely removed when the centrifugal speed reaches its maximum. Therefore, NMR results from samples taken at 12,000 rpm were used to distinguish movable fluid from capillary bound fluid. With an increase in drying temperature, the NMR signal frequency of shale samples decreases to 80 °C and remains unchanged. This suggests that capillary bound fluid is almost completely removed when the drying temperature is above 80 °C. In order to ensure the reliability of the threshold temperature, the NMR results of the samples under the drying condition of 100 °C are used to distinguish capillary bound and unrecoverable fluid.

As shown in Figure 6, the NMR T_2 spectra of shale samples under full brine saturation, 12,000 rpm centrifugation and 100 °C drying conditions were used to calculate NMR porosity, including movable, capillary bound and unrecoverable fluid porosity. The T_2 cutoff value as a boundary distinguishing the relaxation time of movable and capillary bound fluid can be obtained by projecting the cumulative value of the porosity component onto the corresponding relaxation time axis [16]. Table 2 presents the calculation results of the NMR experimental parameters. The movable fluid porosity ranges from 0.88 to 2.99%, with an average value of 2.06%. The capillary bound fluid porosity ranges from 2.61 to 5.80%, with an average value of 3.92%. And the unrecoverable fluid porosity ranges from 0.28 to 0.50%, with an average value of 0.41%. It is shown that the NMR porosity of the shale samples is dominated by capillary bound fluid porosity, while the movable fluid porosity is lower than the capillary bound fluid porosity. This is the main reason why the fluid in the shale has difficulty in flowing, despite the many microfractures. Meanwhile, the T_2 cutoff value ranges from 0.55 ms to 6.73 ms, with an average value of 1.48 ms, which is basically the same order of magnitude as previous research results [16,19,24,26]. The values are about an order of magnitude lower than for tight sandstones and about 1–2 orders

of magnitude lower than for conventional sandstones and carbonate rocks [34,35]. In particular, there is a significant increase in the T_2 cutoff value for shale samples at the bottom of the Longmaxi Formation, which may be caused by differences in porosity and pore structure.

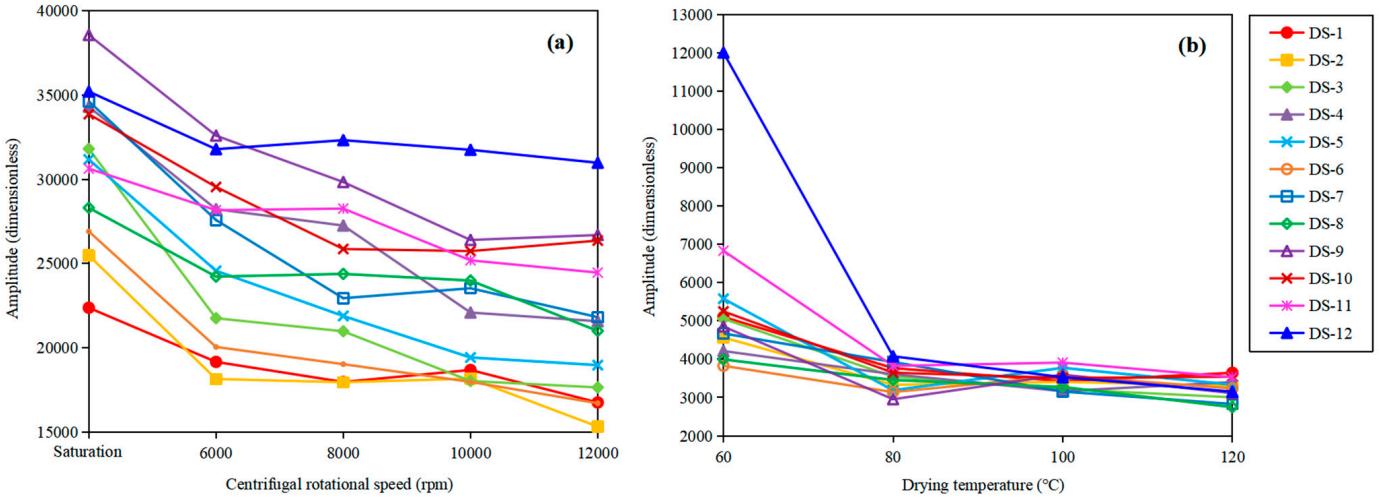

Figure 5. NMR T_2 signal amplitudes of shale samples under different centrifugal rotational speeds (**a**) and drying temperatures (**b**).

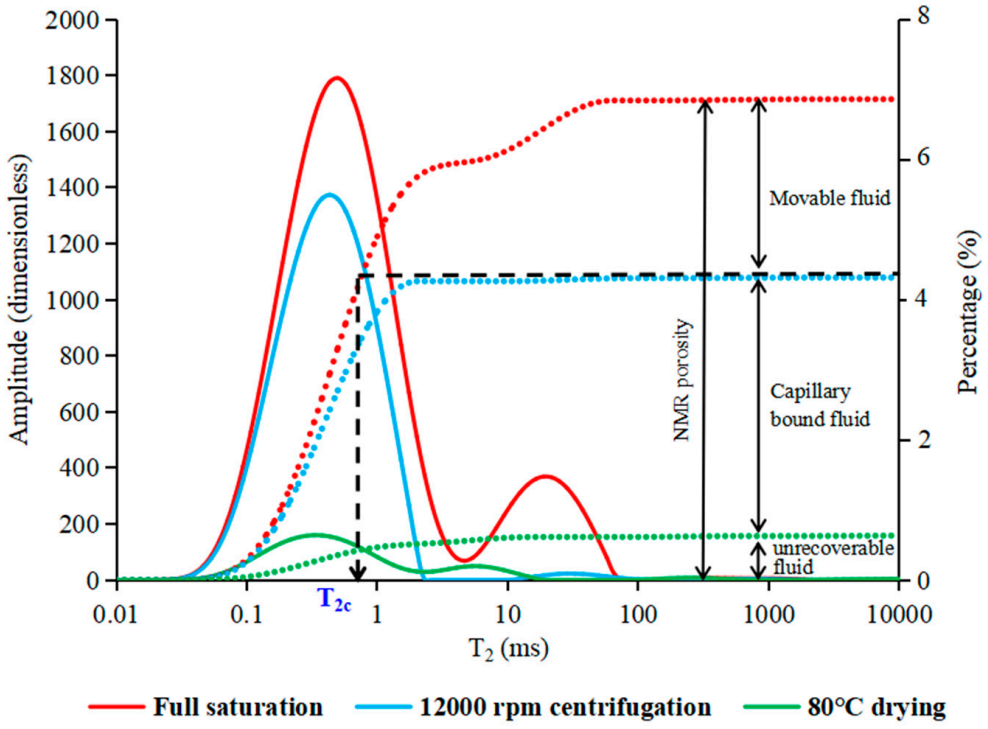

Figure 6. T_2 cutoff value and fluid types of the shale sample DS-4.

Table 2. NMR porosity, T_2 cutoff values and fluid porosity of shale samples.

Sample	φ_{nmr}	φ_{n1}	φ_{n2}	φ_{n3}	T_{2c}
	(%)				(ms)
DS-1	4.48	1.20	2.83	0.46	1.01
DS-2	5.27	2.21	2.61	0.45	0.58
DS-3	6.38	2.99	3.04	0.36	0.55
DS-4	6.95	2.68	3.88	0.39	0.75
DS-5	6.60	2.69	3.48	0.43	0.65
DS-6	5.96	2.36	3.14	0.46	0.68
DS-7	6.83	2.63	3.90	0.31	0.71
DS-8	5.43	1.47	3.68	0.28	1.00
DS-9	8.63	2.74	5.48	0.41	1.37
DS-10	6.69	1.54	4.69	0.46	1.77
DS-11	6.39	1.34	4.55	0.50	1.93
DS-12	7.06	0.88	5.80	0.38	6.73

Note: φ_{nmr} is NMR porosity, %; φ_{n1}, φ_{n2}, φ_{n3} are movable fluid porosity, capillary bound fluid porosity and unrecoverable fluid porosity, respectively, %; T_{2c} is the T_2 cutoff value, %.

4.2. Full-Scale PSD of Shale

As an important parameter to characterize the pore structure of shale, PSD can be determined by analyzing the relaxation time [17,28]. NMR T_2 analysis can be used to characterize the full-scale PSD of shale samples under the premise that pore morphology is a specific geometry. It can be seen from Equation (3) that there is a certain correlation between NMR T_2 distribution and pore structure, and ρ_2 is an established constant in the single sample. After obtaining the transformation relationship between T_2 and (S/V), the NMR T_2 spectrum can be converted into the PSD. Based on this principle [36], Equation (3) is transformed into:

$$\frac{1}{T_2} = \rho_2 \frac{F_S}{\mathrm{r}} \tag{4}$$

where r is pore radius, which is the ratio of pore surface area to pore volume, μm; F_S is pore shape factor, which is used to distinguish between different shapes or types of pores; and ρ_2 is surface relaxivity, μm/ms.

In the process of using FS, it is necessary to make further judgments based on the different types of pores and their morphology. It is generally believed that the F_S of standard circular pores is 3. Due to the FE-SEM observations, the shale samples have many irregular pores and certain connectivity between pores (Figure 4), which is approximately tubular or cylindrical, so F_S is 2 in this study. The surface relaxivity can be calculated by using the capillary pressure generated by the centrifugation experiment, which can be calculated by the following formula [37,38]:

$$P_C = 1.096 \times 10^{-6} \times \Delta\rho \times N^2 \times (R_e - \frac{L}{2}) \times L \tag{5}$$

$$P_C = \frac{2\sigma \cos\theta}{\mathrm{r}} \tag{6}$$

where P_C is centrifugal pressure, MPa; $\Delta\rho$ is the density difference of the centrifugal test two-phase fluid (brine and air), 1.117 g/mL; N is centrifugal speed, 12,000 rpm; R_e is centrifugal radius, 8.8 cm; L is the length of the shale plunger sample, cm; σ is the interfacial tension between air and water, 72 mN/m; and θ is the wetting angle, defined as almost complete wetting, 0°.

Equation (5) was used to calculate the centrifugal pressure of the shale samples during centrifugation at 12,000 rpm, and then Equations (4) and (6) were used to calculate the centrifugal radius and surface relaxivities. The results of the calculations are shown in Table 3. The centrifugal radius ranges from 0.0421 μm to 0.0468 μm and the surface relaxivities range from 0.0032 μm/ms to 0.0391 μm/ms. It can be seen that the difference in

centrifugal radius between the different shale samples is small, but the difference in surface relaxivity is relatively great. It is believed that the low surface relaxivity of shale is caused by a high content of siliceous minerals [26]. As can be seen from Figure 7, the T_2 cutoff value is positively correlated with TOC and quartz content and negatively correlated with clay mineral content, while the correlation law for the surface relaxivity is the opposite. The shale at the bottom of the Longmaxi Formation is characterized by high quartz and TOC content. Meanwhile, its T_2 cutoff values are relatively high and its surface relaxation rates are relatively low. This indicates that the siliceous mineral and TOC content control the pore type and structure of the shale, resulting in a difference between the T_2 cutoff value and the surface relaxivity distribution.

Table 3. He porosity and centrifugal experimental parameters of shale samples.

Sample	L	V	φ_{He}	P_c	r	ρ_2
	(cm)	(cm^3)	(%)	(MPa)	(μm)	(μm/ms)
DS-1	2.48	12.57	2.94	33.03	0.0436	0.0216
DS-2	2.43	12.30	3.72	32.51	0.0443	0.0382
DS-3	2.52	12.78	4.29	33.49	0.0430	0.0391
DS-4	2.51	12.70	4.43	33.33	0.0432	0.0288
DS-5	2.40	12.14	4.40	32.21	0.0447	0.0344
DS-6	2.28	11.55	4.22	30.77	0.0468	0.0344
DS-7	2.57	13.03	4.60	34.04	0.0423	0.0298
DS-8	2.62	13.28	3.73	34.62	0.0416	0.0208
DS-9	2.29	11.58	5.60	30.90	0.0466	0.0170
DS-10	2.57	13.01	4.51	34.20	0.0421	0.0119
DS-11	2.43	12.30	5.12	32.43	0.0444	0.0115
DS-12	2.54	12.84	5.86	33.41	0.0431	0.0032

Note: L is the length of shale samples, cm; V is the volume of shale samples, cm^3; φ_{He} is the He porosity of shale samples, %.

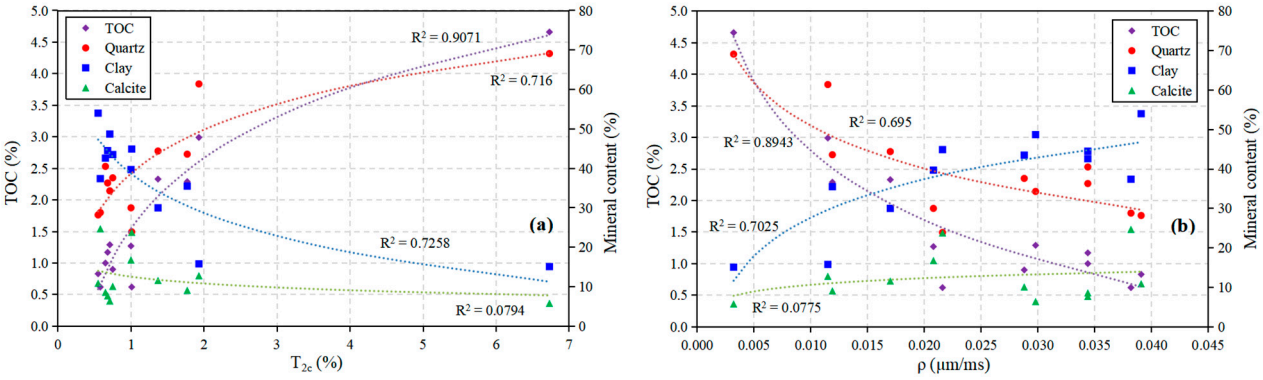

Figure 7. Correlation of T_2 cutoff values (**a**) and surface relaxivities (**b**) with TOC content and mineral content of shale samples.

Equation (4) is further used to calculate the full-scale PSD of shale samples. During the calculation, the NMR signal of the unrecoverable fluid needs to be removed. Figure 8 shows that the overall pore radii of the shale samples mainly range from 1 nm to 5000 nm. According to the classification scheme for shale pore size, pores can be divided into macropores (pore diameter > 1000 nm), mesopores (1000 nm > pore diameter > 100 nm), transition pores (100 nm > pore diameter > 10 nm) and micropores (10 nm > pore diameter) [32]. In this study, shale pores are mainly distributed in the range of 1 nm to 200 nm, belonging to micropores and transition pores. Microfractures are mainly distributed between 200 nm and 5000 nm, belonging to mesopores and macropores.

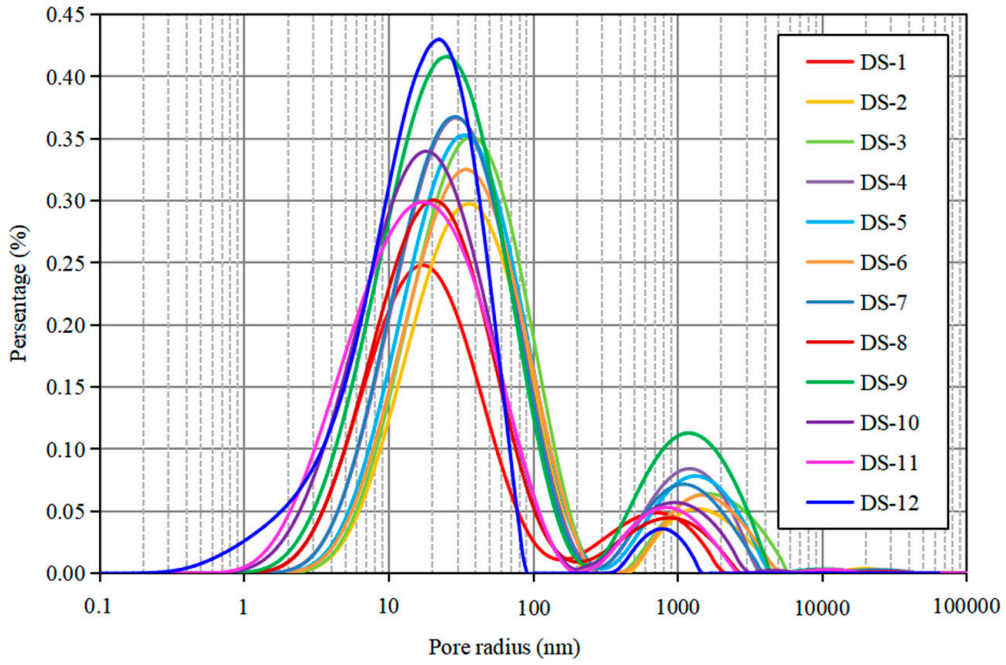

Figure 8. Full-scale pore size distribution of shale samples.

4.3. Types and Quantification of Pores and Microfractures

Types of pores and microfractures are critical for the evaluation of shale gas reservoir space [20,21,32,39]. From the images, the development degree of organic pores in the Longmaxi Formation shale is much higher than that of inorganic pores (Figures 4 and 9). Specifically, a small number of visible intergranular pores are mainly developed at the edge of isolated mineral particles. The pore morphology is amorphous under the extrusion of mineral particles, and the pore size is distributed at 20–300 nm (Figure 4c,d). Organic pores are mainly spongy and developed inside organic matter, with pore sizes in the range of 5–800 nm. There is a certain connectivity among pores, and the connectivity of macropores is better than that of micropores (Figure 4g,h,k,l). However, the development characteristics of pores in different types of organic matter are slightly different. Algae and bioclasts are generally larger than 10 μm and have a certain biological structure in morphology. Solid asphalt particles are generally smaller than 10 μm and have no specific morphology [17]. Pores inside algae are uneven in size, and some of them are jagged (Figure 9a,b). Sponge spicule pores are generally small and dense (Figure 9c,d). Solid bitumen pores are generally large and have good connectivity (Figure 9e,f). Similarly, these organic pores are nano-sized and are mostly surrounded by rigid minerals such as quartz and calcite (Figure 9a,c,e,f). The supporting structure of these rigid minerals facilitates the preservation of organic pores during deep burial.

Figure 10 shows three types of microfractures in shale, including bedding fractures, mineral filling fractures and structural fractures. Bedding fractures are generally distributed horizontally along the bedding direction and can be up to millimeters in length. Filling fractures contain calcite formed by the intrusion of hydrothermal fluid after diagenesis, with a length of 5–40 μm. Structural fractures may be formed by shrinkage of clay minerals after dehydration, and are 1–10 μm in length. On the whole, these microfractures are generally larger than 1 μm and serve as effective channels for fluid migration.

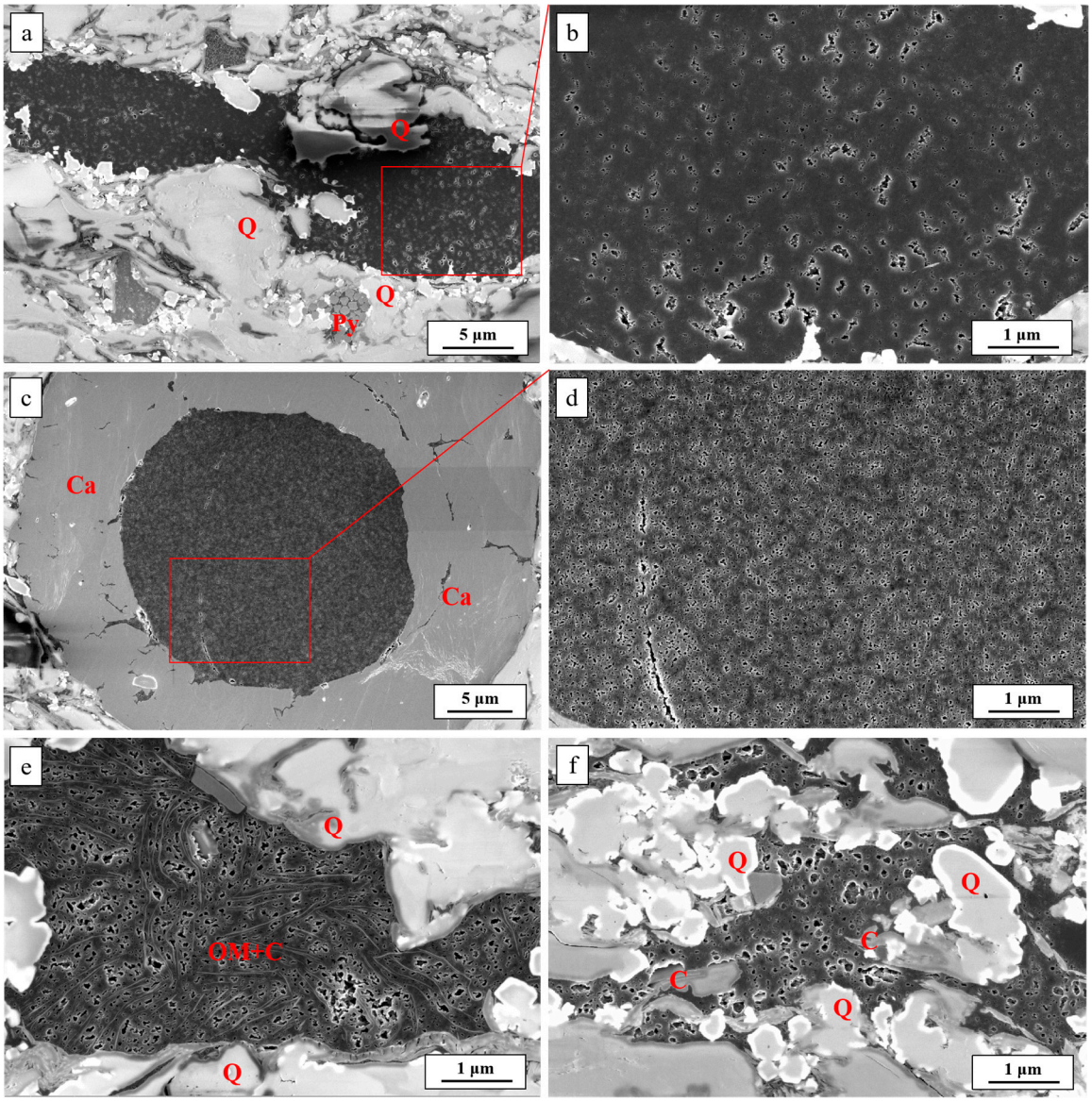

Figure 9. (**a**–**f**) FE-SEM images of organic pores in shale samples. (Q: quartz; Py: pyrite; Ca: calcite; C: clay; OM: organic matter).

Based on the identification of NMR T_2 spectra, PSD parameters can be used to quantitatively calculate pores and microfractures of shale [20]. As shown in Figure 11, the lowest r_1 value between the two peaks was found to be the boundary value to determine the peak location of the pore and microfracture. Then, using the functional relationship between pore size and porosity, the porosity occupied by pores and microfractures is calculated by definite integration:

$$\phi_{\mathrm{np}} = \int_{r_{\min}}^{r_1} f(r)dr \tag{7}$$

$$\phi_{\mathrm{nf}} = \int_{r_1}^{r_{\max}} f(r)dr \tag{8}$$

where φ_{np} is pore content, %; φ_{nf} is microfracture content, %; and r_1 is the horizontal value of the lowest point between the two peaks of PSD.

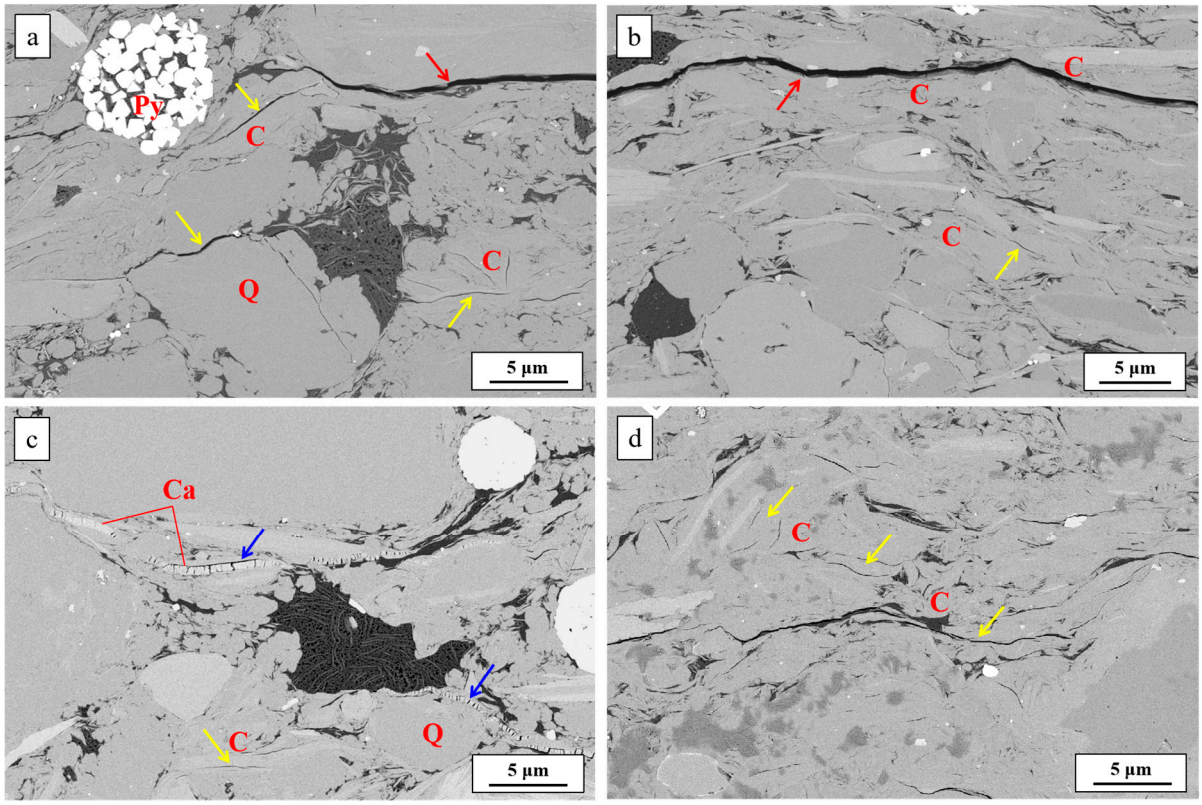

Figure 10. (**a**–**d**) FE-SEM images of microfractures in shale samples. Yellow arrows point to bedding fractures, blue arrows point to mineral filling fractures and red arrows point to structural fractures. Q: quartz; Py: pyrite; Ca: calcite; C: clay.

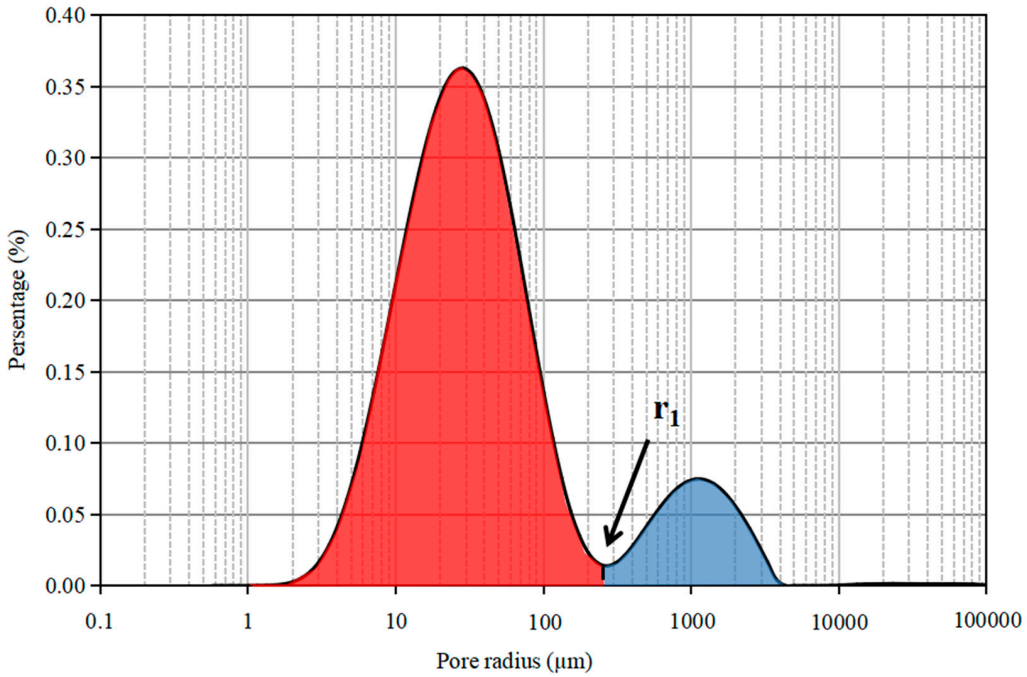

Figure 11. Pores and microfractures of shale samples are quantitatively distinguished based on the full-scale pore size distribution. The red area represents the pores and the blue area represents the microfractures.

After calculation, the pore content of shale samples has a range of 3.44–6.79%, and the microfracture content ranges from 0.22 to 1.43% (Table 4). Theoretically, although there is a certain connectivity between shale pores, the mobility of pore fluid is poor. As can be seen from Figure 9, although the pore sizes of some organic pores are much larger than the average mechanical centrifugal radius, centrifugation still fails to remove the fluid in these pores. This is because the connectivity between the pores is based on small throats, resulting in the fluid being subjected to a capillary force greater than centrifugal pressure. Meanwhile, organic matter also developed isolated small pores (Figure 9), and the internal fluid in these pores may be unrecoverable fluid. It is believed that the continuity of NMR T_2 spectral peaks is related to the connectivity of pores [16]. Poor continuity of the T_2 spectral peaks of the shale samples in the brine saturated state (Figure 3) indicates that the connectivity between pores and microfractures is limited.

Table 4. Calculation parameters of pores and microfractures of shale samples.

Sample	r_1	φ_{np}	φ_{nf}
	(nm)	(%)	
DS-1	151.7	3.44	0.58
DS-2	308.4	4.26	0.56
DS-3	315.7	5.25	0.77
DS-4	267.4	5.64	0.92
DS-5	319.3	5.28	0.89
DS-6	319.3	4.83	0.67
DS-7	276.6	5.69	0.83
DS-8	193.1	4.62	0.54
DS-9	239.9	6.79	1.43
DS-10	193.0	5.56	0.67
DS-11	214.5	5.33	0.56
DS-12	182.3	6.46	0.22

By comparing the fluid mobility of pores and microfractures in the shale samples, pore content has a positive correlation with capillary bound fluid porosity (Figure 12a), while microfracture content has a positive correlation with movable fluid porosity (Figure 12b), indicating that pore fluid type is basically dominated by capillary bound fluid and microfractures are obviously more conducive to fluid migration. Furthermore, pore content has a positive correlation with quartz and TOC content (Figure 12c), while microfracture content has no significant correlation with mineral content (Figure 12d). These results indicate that siliceous mineral and TOC content play a major role in controlling the pore content of shale, while microfractures are less affected by them. This may be because the origin and types of microfractures are relatively complex.

4.4. Difference between NMR Porosity and He Porosity

The difference between NMR porosity and He porosity is easily missed due to the different testing methods. Some previous research results [16,23,26] showed that shale NMR porosity is generally higher than He porosity (Figure 13a), which affects the validity of the NMR analysis results of shale. This may be caused by the following reasons: (1) In the process of shale saturation in aqueous solution, clay minerals easily absorb water and deform, resulting in some extra pores and microfractures [29,40–42]. (2) There are some natural or artificial microfractures in shale, which cannot be detected by gas logging porosity measurement. (3) The NMR signals of unrecoverable fluid in shale and hydrogen in organic matter cannot be eliminated [24,43]. (4) Paramagnetic minerals such as Fe^{3+} and Mn^{2+} in shale will form noise signals and interfere with the results of NMR measurement [25,44,45].

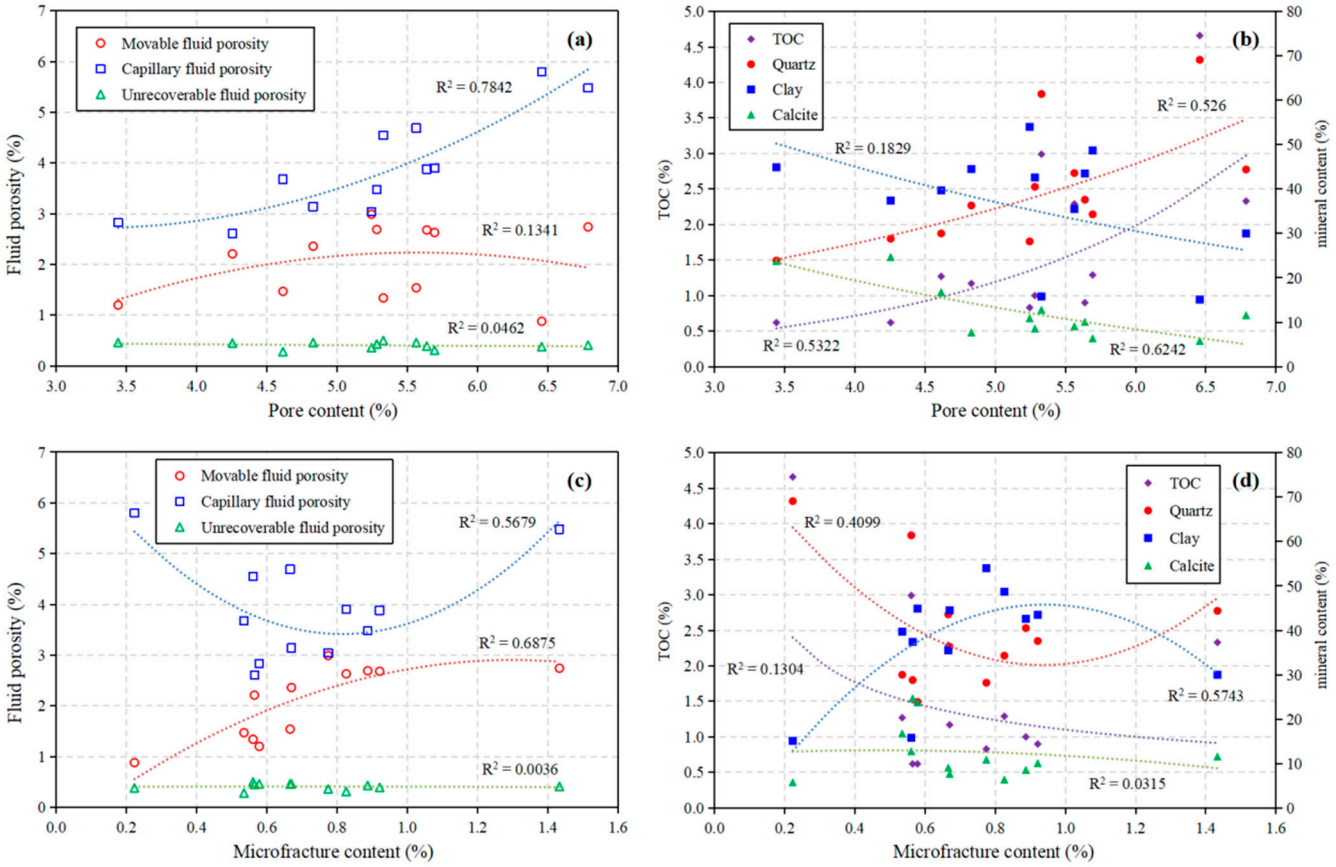

Figure 12. Correlation of pore content (**a**,**b**) and microfracture content (**c**,**d**) with fluid porosity and mineral content of shale samples.

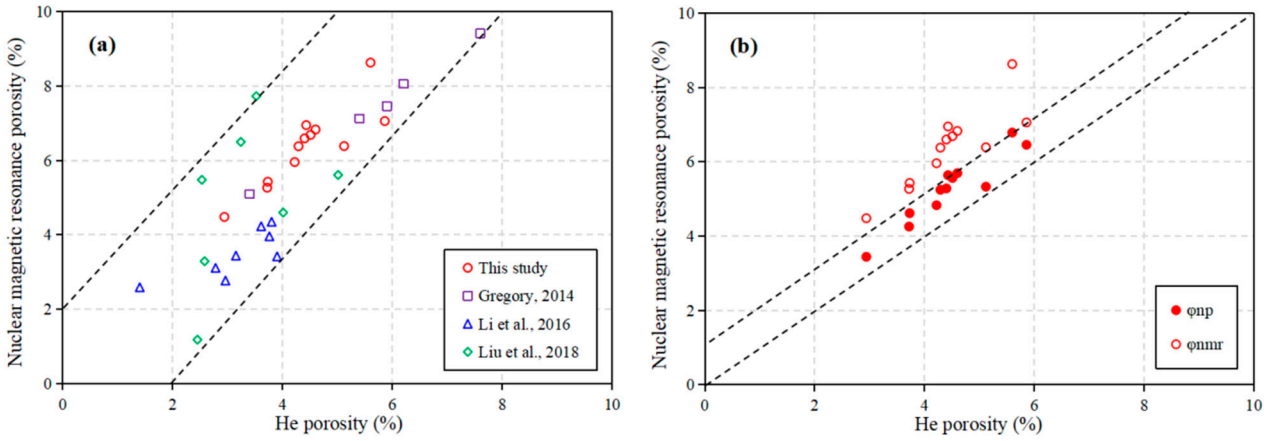

Figure 13. Correlation between NMR porosity and He porosity of shale [16,23,26]. (**a**) Previous studies and this study; (**b**) difference between φ_{nmr} and φ_{np}.

In this study, NMR porosity of all shale samples is also higher than He porosity (Figure 12a). However, the pore content calculated using the PSD parameter has a good matching relationship with He porosity (Figure 13b). This indicates that gas logging porosity is primarily used to detect connected pores in shale, but NMR can also be used to analyze closed pores, microfractures and fluid distribution. Therefore, NMR techniques are more comprehensive in shale reservoir characterization. Further work will be carried out to investigate the pore structure characterization of shale under simulated formation conditions by using NMR and high-temperature pressure displacement experimental facilities.

5. Conclusions

In this paper, the pores and microfractures of twelve shale samples from the Lower Silurian Longmaxi Formation in southeast Sichuan Basin are quantitatively characterized using NMR experiments. Moreover, the type and distribution characteristics of the shale reservoir space are systematically analyzed and the validity of the NMR experimental results are discussed. The following conclusions can be drawn.

(1) The NMR T_2 spectra of shale samples in full brine saturation is characterized by a bimodal distribution. The left peak has a shorter relaxation time corresponding to the pores, and the right peak has a longer relaxation time corresponding to the microfractures. The two peaks have ranges of 0.01–20 ms and 3–300 ms, respectively. Shale reservoir space is dominated by nanoscale organic pores, with inorganic pores and microfractures contributing much less than organic pores.

(2) The movable, capillary bound and unrecoverable fluids of shale are distinguished by NMR T_2 spectra under the conditions of fully saturated brine, 12,000 rpm centrifugation and 100 °C drying. The results show that the fluid in the shale is mainly capillary bound fluid, which is the main reason for the difficulty in pore fluid migration.

(3) The T_2 cutoff value of shale is 0.55–6.73 ms, and the surface relaxivity is 0.0032–0.0391 μm/ms. There is a strong correlation between these two parameters and TOC, suggesting that organic matter is the main factor controlling the pore type and pore structure of shale.

(4) The full-scale PSD of the shale shows a pore range of 1–200 nm and a microfracture range of 200–5000 nm. The main forms of fluid in the pores and microfractures are capillary bound fluid and movable fluid, respectively, and the corresponding NMR porosity ranges are 3.44–6.79% and 0.22–1.43%, respectively.

(5) NMR porosity of the shale is generally higher than He porosity. The reason for this is that gas logging pore analysis is mainly used to detect connected pores in shale, whereas NMR analysis also includes information about closed pores and microfractures.

Author Contributions: Formal analysis, B.S. and L.L.; Data curation, A.P., Z.L. and Q.Z.; Writing—original draft, C.L.; Supervision, Z.S. All authors have read and agreed to the published version of the manuscript.

Funding: This research was funded by Enterprise Innovation and Development Joint Fund of National Natural Science Foundation of China "Enrichment regularity and development mechanism of deep marine shale gas (U19B600303)" and SINOPEC Science and Technology Department Project "Research on Precision Characterization of Shale Pore and Fluid Dynamic Monitoring Technology (P20059-8)".

Institutional Review Board Statement: Not applicable.

Informed Consent Statement: Not applicable.

Data Availability Statement: The data is unavailable due to privacy.

Conflicts of Interest: The authors declare no conflict of interest.

References

1. Ma, Y.S.; Cai, X.Y.; Zhao, P.R. China's shale gas exploration and development: Understanding and practice. *Pet. Explor. Dev.* **2018**, *45*, 589–603. [CrossRef]
2. Jarvie, D.M.; Hill, R.J.; Ruble, T.E.; Pollastro, R.M. Unconventional shale-gas systems: The Mississippian Barnett Shale of north-central Texas as one model for thermogenic shale-gas assessment. *AAPG Bull.* **2007**, *91*, 475–499. [CrossRef]
3. Loucks, R.G.; Reed, R.M.; Ruppel, S.C.; Jarvie, D.M. Morphology, genesis, and distribution of nanometer-scale pores in siliceous mudstones of the Mississippian Barnett Shale. *J. Sediment. Res.* **2009**, *79*, 848–861. [CrossRef]
4. Loucks, R.G.; Reed, R.M.; Ruppel, S.C.; Hammes, U. Spectrum of pore types and networks in mudrocks and a descriptive classification for matrix-related mudrock pores. *AAPG Bull.* **2012**, *96*, 1071–1098. [CrossRef]
5. Slatt, R.M.; O'Brien, N.R. Pore types in the Barnett and Woodford gas shales: Contribution to understanding gas storage and migration pathways in fine-grained rocks. *AAPG Bull.* **2011**, *95*, 2017–2030. [CrossRef]

6. Yang, R.; He, S.; Yi, J.Z.; Hu, Q.H. Nano-scale pore structure and fractal dimension of organic-rich Wufeng-Longmaxi shale from Jiaoshiba area, Sichuan Basin: Investigations using FE-SEM, gas adsorption and helium pycnometry. *Mar. Pet. Geol.* **2016**, *70*, 27–45. [CrossRef]
7. Li, Z.; Lei, Z.; Shen, W.; Martyushev, D.A.; Hu, X. A Comprehensive Review of the Oil Flow Mechanism and Numerical Simulations in Shale Oil Reservoirs. *Energies* **2023**, *16*, 3516. [CrossRef]
8. Maex, K.; Baklanov, M.R. Porous low dielectric constant materials for microelectronics. *J. Appl. Phys.* **2003**, *93*, 8793–8841. [CrossRef]
9. Jop, K.; Guillaume, D.; Janos, L.U.; Ralf, L. BIB-SEM study of the pore space morphology in early mature Posidonia Shale from the Hils area. *Ger. Int. J. Coal Geol.* **2012**, *103*, 12–25.
10. Martyushev, D.A.; Ponomareva, I.N.; Chukhlov, A.S.; Davoodi, S.; Osovetsky, B.M.; Kazymov, K.P.; Yang, Y. Study of void space structure and its influence on carbonate reservoir properties: X-ray microtomography, electron microscopy, and well testing. *Mar. Pet. Geol.* **2023**, *151*, 106192. [CrossRef]
11. Yang, F.; Ning, Z.F.; Hu, C.P.; Wang, B.; Peng, K.; Liu, H.Q. Characterization of microscopic pore structures in shale reservoirs. *Acta Pet. Sin.* **2013**, *34*, 301–311. (In Chinese)
12. Tian, H.; Pan, L.; Xiao, X.M.; Wilkins, R.W.T.; Meng, Z.P.; Huang, B.J. A preliminary study on the pore characterization of Lower Silurian black shales in the Chuandong Thrust Fold Belt, southwestern China using low pressure N_2 adsorption and FE-SEM methods. *Mar. Pet. Geol.* **2013**, *48*, 8–19. [CrossRef]
13. Xi, Z.D.; Tang, S.H.; Wang, J.; Yang, G.Q.; Li, L. Formation and development of pore structure in marine-continental transitional shale from northern China across a maturation gradient: Insights from gas adsorption and mercury intrusion. *Int. J. Coal Geol.* **2018**, *200*, 87–102. [CrossRef]
14. Yao, Y.B.; Liu, D.M.; Cai, Y.D.; Li, J.Q. Advanced characterization of pores and fractures in coals by nuclear magnetic resonance and X-ray computed tomography. *Sci. China Earth Sci.* **2010**, *53*, 854–862. [CrossRef]
15. Sigal, R.F. Pore-Size Distributions for Organic-Shale-Reservoir Rocks From Nuclear-Magnetic-Resonance Spectra Combined with Adsorption Measurements. *SPE J.* **2015**, *20*, 824–830. [CrossRef]
16. Li, A.; Ding, W.L.; Wang, R.R.; He, J.H.; Wang, X.H.; Sun, Y.X.; Gu, Y.; Jiao, N.L. Petrophysical characterization of shale reservoir based on nuclear magnetic resonance (NMR) experiment: A case study of Lower Cambrian Qiongzhusi Formation in eastern Yunnan Province, South China. *J. Nat. Gas Sci. Eng.* **2017**, *37*, 29–38. [CrossRef]
17. Zhao, P.Q.; Wang, L.; Xu, C.H.; Fu, J.H.; Shi, Y.J.; Mao, Z.Q.; Xiao, D.S. Nuclear magnetic resonance surface relaxivity and its advanced application in calculating pore size distributions. *Mar. Pet. Geol.* **2020**, *111*, 66–74. [CrossRef]
18. Fu, Y.H.; Jiang, Y.Q.; Dong, D.Z.; Hu, Q.H.; Lei, Z.A.; Peng, H.; Gu, Y.F.; Ma, S.G.; Wang, Z.M.; Yin, X.P.; et al. Microscopic pore-fracture configuration and gas-filled mechanism of shale reservoirs in the western Chongqing area, Sichuan Basin, China. *Pet. Explor. Dev.* **2021**, *48*, 1063–1076. [CrossRef]
19. Yao, Y.B.; Liu, D.M.; Che, Y.; Tang, D.Z.; Tang, S.H.; Huang, W.H. Petrophysical characterization of coals by low-field nuclear magnetic resonance (NMR). *Fuel.* **2010**, *89*, 1371–1380. [CrossRef]
20. Wang, Z.Z.; Qin, L.M.; Lu, H.S.; Li, X.; Du, H.F.; Gai, S.S.; Niu, Q.; Yang, P.Q. Two dimentional NMR analysis and evaluation of oil or gas shale. In Proceedings of the SPE 176184, SPE/IATMI Asia Pacific Oil & Gas Conference and Exhibition, Bali, Indonesia, 20–22 October 2015.
21. Zeng, Y.J.; Pang, Y.; Ding, S.D.; Di, K.X.; Shen, Z.Q.; Chen, S.N. Pore-fracture network alteration during forced and spontaneous imbibition processes in shale formation. *J. Pet. Sci. Eng.* **2022**, *209*, 109846. [CrossRef]
22. Xu, M.; Dehghanpour, H. Advances in understanding wettability of gas shales. *Energy Fuels* **2014**, *28*, 4362–4375. [CrossRef]
23. Gannaway, G. NMR investigation of pore structure in gas shales. In Proceedings of the SPE 173474, SPE Annual Technical Conference and Exhibition, Amsterdam, The Netherlands, 27–29 October 2014.
24. Jiang, Y.Q.; Liu, X.W.; Fu, Y.H.; Chen, H.; Zhang, H.J.; Yan, J.; Chen, C.; Gu, Y.F. Evaluation of effective porosity in marine shale reservoir, western Chongqing. *Acta Pet. Sin.* **2019**, *40*, 1233–1243. (In Chinese)
25. Livo, K.; Saidian, M.; Prasad, M. Effect of paramagnetic mineral content and distribution on nuclear magnetic resonance surface relaxivity in organic-rich Niobrara and Haynesville shales. *Fuel* **2020**, *269*, 117417. [CrossRef]
26. Liu, Y.; Yao, Y.B.; Liu, D.M.; Zheng, S.J.; Sun, G.X.; Chang, Y.H. Shale pore size classification: An NMR fluid typing method. *Mar. Pet. Geol.* **2018**, *96*, 591–601. [CrossRef]
27. Straley, C.; Rossini, D.; Vinegar, H.; Tutunjian, P.; Morriss, C. Core analysis by low field NMR. *Log. Anal.* **1997**, *38*, 84–93.
28. Coates, G.R.; Xiao, L.Z.; Prammer, M.G. *NMR Logging Principles and Applications*; Gulf Publishing Company: Houston, TX, USA, 1999.
29. Tinni, A.; Odusina, E.; Sulucarnain, I.; Sondergeld, C.R. NMR response of brine, oil and methane in organic rich shales. In Proceedings of the SPE 168971, SPE Unconventional Resources Conference, The Woodlands, TX, USA, 1–3 April 2014.
30. Wei, X.F.; Liu, Z.J.; Wang, Q.; Wei, F.B.; Yuan, T. Analysis and thinking of the difference of Wufeng-Longmaxi shale gas enrichment conditions between Dingshan and Jiaoshiba areas in southeastern Sichuan Basin. *Nat. Gas Geosci.* **2020**, *31*, 1041–1051. (In Chinese)
31. Lu, L.F.; Qin, J.Z.; Shen, B.J.; Tenger Liu, W.X.; Zhang, Q.Z. The origin of biogenic silica in siliceous shale from Wufeng-Longmaxi Formation in the Middle and Upper Yangtze region and its relationship with shale gas enrichment. *Earth Sci. Front.* **2018**, *25*, 226–236. (In Chinese)
32. Curtis, J.B. Fractured shale-gas system. *AAPG Bull.* **2002**, *86*, 1921–1938.

33. Testamanti, M.N.; Rezaee, R. Determination of NMR T_2 cut-off for clay bound water in shales: A case study of Carynginia Formation, Perth Basin, Western Australia. *J. Pet. Sci. Eng.* **2017**, *149*, 497–503. [CrossRef]
34. Wang, W.M.; Ye, C.H.; Guo, H.K. Experimental studies of NMR properties of continental sedimentary rocks. *Chin. J. Magn. Reson.* **2001**, *18*, 113–121. (In Chinese)
35. Ding, W.L.; Fan, T.L.; Yu, B.S.; Huang, X.B.; Liu, C. Ordovician carbonate reservoir fracture characteristics and fracture distribution forecasting in the Tazhong Area of Tarim Basin, Northwest China. *J. Pet. Sci. Eng.* **2012**, *86–87*, 62–70. [CrossRef]
36. Sondergeld, C.H.; Ambrose, R.J.; Rai, C.S.; Moncrieff, J. Micro-structural studies of gas shales. In Proceedings of the SPE 131771, SPE Unconventional Gas Conference, Pittsburgh, PA, USA, 23–25 February 2010.
37. Tiab, D.; Donaldson, E.C. *Petrophysics: Theory and Practice of Measuring Reservoir Rock and Fluid Transport Properties*; Gulf Professional Publishing: Houston, TX, USA, 2012.
38. Karimi, S.; Kazemi, H. Capillary pressure measurement using reservoir fluids in a Middle Bakken Core. In Proceedings of the SPE 174065, SPE Western Regional Meeting, Garden Grove, CA, USA, 27–30 April 2015.
39. Li, L.; Sheng, G.; Su, Y. Water-Gas Two-Phase Flow Behavior of Multi-Fractured Horizontal Wells in Shale Gas Reservoirs. *Processes* **2019**, *7*, 664. [CrossRef]
40. Roshan, H.; Ehsani, S.; Marjo, C.E.; Andersen, M.S.; Acworth, R.I. Mechanisms of water adsorption into partially saturated fractured shales: An experimental study. *Fuel* **2015**, *159*, 628–637. [CrossRef]
41. Xue, H.Q.; Zhou, S.W.; Jiang, Y.l.; Zhang, F.D.; Dong, Z.; Guo, W. Effects of hydration on the microstructure and physical properties of shale. *Pet. Explor. Dev.* **2018**, *45*, 1146–1153. [CrossRef]
42. Yang, L.; Dou, N.H.; Lu, X.B.; Zhang, X.H.; Chen, X.; Gao, J.; Yang, C.W.; Wang, Y. Advances in understanding imbibition characteristics of shale using an NMR technique: A comparative study of marine and continental shale. *J. Geophys. Eng.* **2018**, *15*, 1363–1375. [CrossRef]
43. Khatibi, S.; Ostadhassan, M.; Xie, Z.H.; Gentzis, T.; Bubach, B.; Gan Zheng Carvajal-Ortiz, H. NMR relaxometry a new approach to detect geochemical properties of organic matter in tight shales. *Fuel* **2019**, *235*, 167–177. [CrossRef]
44. Saidian, M.; Prasad, M. Effect of mineralogy on nuclear magnetic resonance surface relaxivity: A case study of Middle Bakken and Three Forks formations. *Fuel* **2015**, *161*, 197–206. [CrossRef]
45. Liu, Z.S.; Liu, D.M.; Karacan, C.; Cai, Y.D.; Yao, Y.B.; Pan, Z.J.; Zhou, Y.F. Application of nuclear magnetic resonance (NMR) in coalbed methane and shale reservoirs: A review. *Int. J. Coal Geol.* **2020**, *218*, 203261. [CrossRef]